

Application of Structure-from-Motion photogrammetry in laboratory flumes



Jacob A. Morgan*, Daniel J. Brogan, Peter A. Nelson

Department of Civil and Environmental Engineering, Colorado State University, 1372 Campus Delivery, Fort Collins, CO 80523-1372, USA

ARTICLE INFO

Article history:

Received 6 July 2016

Received in revised form 10 October 2016

Accepted 11 October 2016

Available online 14 October 2016

Keywords:

Structure-from-Motion (SfM)

Terrestrial laser scanning (TLS)

Laboratory flume methods

Close-range photogrammetry

Topographic modeling

ABSTRACT

Structure-from-Motion (SfM) photogrammetry has become widely used for topographic data collection in field and laboratory studies. However, the relative performance of SfM against other methods of topographic measurement in a laboratory flume environment has not been systematically evaluated, and there is a general lack of guidelines for SfM application in flume settings. As the use of SfM in laboratory flume settings becomes more widespread, it is increasingly critical to develop an understanding of how to acquire and process SfM data for a given flume size and sediment characteristics. In this study, we: (1) compare the resolution and accuracy of SfM topographic measurements to terrestrial laser scanning (TLS) measurements in laboratory flumes of varying physical dimensions containing sediments of varying grain sizes; (2) explore the effects of different image acquisition protocols and data processing methods on the resolution and accuracy of topographic data derived from SfM techniques; and (3) provide general guidance for image acquisition and processing for SfM applications in laboratory flumes. To investigate the effects of flume size, sediment size, and photo overlap on the density and accuracy of SfM data, we collected topographic data using both TLS and SfM in five flumes with widths ranging from 0.22 to 6.71 m, lengths ranging from 9.14 to 30.48 m, and median sediment sizes ranging from 0.2 to 31 mm. Acquisition time, image overlap, point density, elevation data, and computed roughness parameters were compared to evaluate the performance of SfM against TLS. We also collected images of a pan of gravel where we varied the distance and angle between the camera and sediment in order to explore how photo acquisition affects the ability to capture grain-scale microtopographic features in SfM-derived point clouds. A variety of image combinations and SfM software package settings were also investigated to determine optimal processing techniques. Results from this study suggest that SfM provides topographic data of similar accuracy to TLS, at higher resolution and lower cost. We found that about 100 pixels per grain are required to resolve grain-scale topography. We suggest protocols for image acquisition and SfM software settings to achieve best results when using SfM in laboratory settings. In general, convergent imagery, taken from a higher angle, with at least several overlapping images for each desired point in the flume will result in an acceptable point cloud.

© 2016 Elsevier B.V. All rights reserved.

1. Introduction

High-resolution topographic data collected during mobile-bed flume experiments has led to important advances in our scientific understanding of fundamental processes in river morphodynamics. For example, differencing successive topographic datasets can be used to quantify the formation and migration of alternate bars (Lisle et al., 1993; Lanzoni, 2000a,b; Venditti et al., 2012), the translation and dispersion of sediment pulses (Sklar et al., 2009; Humphries et al., 2012; Nelson et al., 2015), the formation and migration of

meanders (Braudrick et al., 2009; van Dijk et al., 2012), and patterns of bedrock erosion (Johnson and Whipple, 2007; Finnegan et al., 2007). High-resolution topographic data can also provide important information about streambed structure (Aberle and Nikora, 2006), bed roughness, (Qin and Ng, 2012), and bed surface grain size (Butler et al., 2001; Nelson et al., 2010).

It generally is impractical to acquire dense topographic data manually using instruments such as point gages (Gilbert and Murphy, 1914; Brush and Wolman, 1960; Schumm and Khan, 1972). Thus, many modern flumes are outfitted with computer-controlled, mechanized instrumentation carts mounted with laser profilers (Marion et al., 2003; Aberle and Nikora, 2006; Nelson et al., 2010, 2009; Kim et al., 2015) and ultrasonic sensors (Kuhnle, 1993; Venditti et al., 2015). Cart-based measurement systems can be prohibitively expensive

* Corresponding author.

E-mail address: jacob.morgan@colostate.edu (J. Morgan).

because such systems are generally highly customized and require high precision instrumentation to maintain accurate positioning during data collection. Terrestrial laser scanning (TLS), while primarily used in field-based applications (Brasington et al., 2012), has been used in some flume settings for comparative studies (Peter Heng et al., 2010; Smith and Vericat, 2014). TLS systems can, however, be extremely expensive and challenging to set up and use.

Digital photogrammetry provides an alternative to TLS or cart-based systems. Traditional close-range digital photogrammetry generally employs the use of multiple cameras to create 3D models of real space. These methods require either the precise location and angle of the camera position or the location of multiple ground control points in each image captured. Traditional photogrammetry has been successfully used in both the field (e.g., Lane et al., 1993; Marzolff and Poesen, 2009) and laboratory (e.g., Chandler et al., 2001; Brasington and Smart, 2003; Stojic et al., 1998; Lane et al., 2001; Bertin et al., 2015). However, the use of these techniques appears to be limited due to the time required to set up such a system and the degree of expertise necessary for accurate reconstruction of a 3D surface (Smith et al., 2015).

An emerging photogrammetric technique that is gaining momentum in the geosciences is Structure-from-Motion (SfM). The concept behind SfM was introduced in the late 1970s (Ullman, 1979), but has risen to popularity among non-photogrammetrists following the work of Snavely et al. (2006). Structure-from-Motion uses multi-view computer vision methods that detect and match features between images to estimate the three-dimensional structure and camera locations and angles simultaneously (Lowe, 2004). There are a number of free software options for SfM processing (e.g., Bundler (Snavely et al., 2006), VisualSfM (Wu et al., 2011; Wu, 2013), and Autodesk ReMake (Autodesk, 2016)) as well as proprietary software (e.g., Arc3D (Tingdahl and Van Gool, 2011) and Agisoft PhotoScan (Agisoft, 2016a)). Compared with other close-range remote sensing techniques such as TLS and more traditional photogrammetry, SfM is relatively low-cost and straightforward to process.

SfM techniques have already been used and tested in a wide array of field applications (e.g., Westoby et al., 2012; Fonstad et al., 2013; Micheletti et al., 2015), but few studies have used SfM in a laboratory setting (Marra et al., 2014; Kasprak et al., 2015; Ramos et al., 2015; Wang et al., 2016). This technology is becoming increasingly popular, but to our knowledge there have been no studies explicitly evaluating the relative performance of SfM against other methods of topographic measurement in a laboratory flume environment (but see Nouwakpo et al. (2014)), and there is a general lack of guidelines for SfM application in flume settings. This is especially problematic because experiments may be conducted in flumes spanning a wide range of physical scales (i.e., widths ranging from a few centimeters to several meters) using sediment ranging from silts or fine sands to large cobbles, and it is not clear how SfM data collection protocols and processing methods should change with flume scale, experimental grain size, or level of detail desired. These issues are all of great interest to experimentalists and therefore the objectives of this study were to: (1) compare the resolution and accuracy of SfM topographic measurements to TLS measurements in laboratory flume experiments of varying scale and grain sizes; (2) explore the effects of different image acquisition protocols and data processing methods on the resolution and accuracy of topographic data derived from SfM techniques; and (3) provide general guidance for image acquisition and processing for SfM applications in laboratory flumes.

2. Methods

For this study, we took advantage of several ongoing flume experiments being conducted at Colorado State University's Engineering Research Center. The flumes used in these experiments have

widths varying from 0.22 m to 6.71 m and lengths from 9.14 m to 30.48 m, and the sediment used in the experiments has median grain sizes ranging from 0.20 mm to 31 mm. For each flume, we collected topographic data with two TLS systems, as well as a series of photographs taken at multiple locations with different camera angles that were later used to generate topographic data with SfM. This allowed us to quantitatively compare 3D point clouds generated from each method, and we can explore how the different image acquisition techniques affect topographic data for different flume scales and grain sizes, as well as how SfM processing techniques affect point cloud characteristics. Additionally images were acquired for sediment in a circular pan from a variety of distances and camera angles, for which a qualitative analysis allowed us to assess the requirements necessary to acquire grain-scale topography.

2.1. Flume descriptions

We collected data in five flumes (summarized in Table 1 and shown in Fig. 1a–e), which for this study we refer to with numbers 1 to 5, where the smallest channel is Flume 1 and the largest is Flume 5. We also collected imagery for a pan filled with gravel (Fig. 1f). The grain size distributions of the sediment mixture in each flume and the pan are shown in Fig. 2.

Flume 1 is a narrow (0.22 m wide), 9.14 m long, rectangular channel that is deeper than it is wide (depth = 0.38 m), with a sediment D_{50} of 1.5 mm. This flume has sinusoidal width variations in the downstream direction, and was used in the experiments described in Nelson et al. (2015). At the time of this study, the sediment bed in this flume exhibited riffle-pool topography, with locally high bed elevations in wide sections of the channel (riffles) and locally low elevations in narrow sections (pools).

Flume 2 is 1.22 m wide and 9.14 m long. It was being used to study processes in steep, coarse-grained rivers, and therefore had the coarsest sediment of any of the flumes in this study with a D_{50} of 31 mm.

Flume 3 is 1.22 m wide and 18.29 m long, with a surface sediment D_{50} of 4.1 mm. This flume was being used to investigate alternate bar dynamics, and at the time of data acquisition this flume had approximately 1.5 alternate bar sequences and noticeable bed surface sorting (e.g., Nelson et al., 2010).

Flume 4 is a wide rectangular basin (4.88 m wide by 15.24 m long) that was being used to study flow and erosion around navigation locks. The sediment in this flume was a relatively well sorted (geometric standard deviation $\sigma_g = 1.67$) gravel ($D_{50} = 6.2$ mm).

Flume 5 is a large rectangular basin (6.71 m wide by 30.48 m long) filled with very well sorted ($\sigma_g = 1.37$) sand with $D_{50} = 0.2$ mm. This basin was being used to perform experiments on braided channels in high sediment supply environments (Ettema et al., 2016), and at the time of data acquisition for this study the bed exhibited many shallow (~1 cm depth) braided channels.

The pan is a circular container (0.39 m diameter) filled with a bi-modal mixture of very fine to coarse gravel. This container was not being used for any other experimentation and is only used in this study to examine the effect of camera distance/angle from the sediment surface. No TLS data were collected for the pan because the level of detail of interest is finer than the accuracy of TLS equipment available to us.

2.2. Data acquisition

2.2.1. TLS

Two TLS systems were used to collect topographic data. The first was a Leica ScanStation HDS3000, which is a time-of-flight style scanner with a stated accuracy of ±6 mm at a distance of 50 m (Leica, 2016). This scanner computes distances using the speed of light by measuring the time from short pulses of light sent from the scanner

Table 1

Dimensions of the flumes used to compare TLS and SfM as well as their grain size distribution medians (D_{50}) and geometric standard deviations (σ_g). These dimensions do not correspond to the dimensions used in the point cloud comparisons.

Flume	Total width (m)	Total length (m)	Approx. depth (m)	D_{50} (mm)	σ_g (mm)
1	0.22	9.14	0.38	1.5	2.74
2	1.22	9.14	0.58	31.0	4.33
3	1.22	18.29	0.66	4.1	2.00
4	4.88	15.24	1.20	6.2	1.67
5	6.71	30.48	0.78	0.2	1.37

until a reflection of the pulse is monitored (Paschotta, 2008). The second scanner was a Faro Focus3D S 120, which is a phase-shift scanner with a stated accuracy of ± 2 mm at a distance of 25 m (Faro, 2011). This scanner sends light with a known sinusoidal power modulation and measures distances by comparing this modulation with the phase of the power modulation that is reflected back to the scanner (Paschotta, 2008). In both cases, scanner accuracy should be better at closer ranges, to a point, since the range of accuracy cannot be any smaller than the laser point itself. Each flume was scanned by both scanners from three separate stations, one at the upstream end, one at the downstream end and one near the middle of the flume. Each scan contained a minimum of five reflective spheres that were used to align and position the three scans for a single flume. For two flumes the TLS stations were located with the instrument tripod on a cart that moves above the flume bed, and for the others the stations were located with the tripod at the bed level of the flume. The distance from the instrument to the flume bed depended on the dimensions of the flume and whether the station was on the flume cart or at the bed level. Scanner height above the bed varied from approximately 1.5 to 4 m, resulting in overall distances generally less than those given for the stated accuracy by the manufacturers. The maximum downward angle of view for each of the scanners is 45° and 27.5°, resulting in ranges from the scanner to the closest scanned points of 2.1 to 5.7 m for the Leica and 1.7 to 4.5 m for the Faro. Point density using any TLS is highly dependent on the parameters defined by the user at the time of acquisition as well as the number of stations; here, we set the resolution of the TLS data acquisition so that measurements had a vertical and horizontal spacing of approximately 1 cm at a distance of 10 m from the instrument. Both Leica ScanStation and Faro Focus3D data were processed using the manufacturer's software, Leica Geosystems Cyclone and Faro SCENE, respectively.

2.2.2. Photographs for SfM

Images were acquired using a Canon EOS Rebel T3i camera with a Canon EF-S 24 mm prime lens. This is a consumer grade DSLR camera capable of capturing images with 18.0 megapixel resolution. We acquired all images in both RAW and JPG formats (RAW file sizes are generally 3–4 times larger than their JPG counterparts), and we performed SfM processing with both file types to investigate the effects of digital image compression. The spacing of photograph locations and the angle of each photograph depended on the dimensions of the flume (Fig. 3a). First, a set of photographs was taken along the flume centerline. These camera positions were at an oblique angle (~45° below horizontal) positioned toward the flume bed pointing in both the upstream and downstream directions. These locations were evenly spaced along the longitudinal axis of the flume. The spacing was determined by the camera height above the bed relative to the flume width (e.g., Flume 1 is very deep relative to its width and therefore had finer spacing than some of the larger flumes (Table 2)). Photographs were also taken from the left and right edges of each flume, and these camera positions were also oriented at a vertically oblique angle (~45°) looking down toward the flume bed. For the

larger flumes (Flumes 4 and 5) camera azimuth angles were set to 0° (directly upstream), 45°, 90° (directly across the flume), 135°, and 180° (directly downstream). For the smaller flumes (Flumes 1, 2, and 3) the side camera angles included 45°, 90° (directly across the flume), and 135°. These camera positions were uniformly spaced along the longitudinal axis at approximately the same locations as were collected for the upstream/downstream images.

The most common parameterization used to characterize the overlap of images in a series or between lines is the percent overlap, particularly for aerial imagery. However, because of the multiple camera angles used in this study the overlap percentage between images is highly variable and difficult to interpret. We therefore used the of number of images in which any point is present as a metric to describe the image overlap. This number of overlapping images can easily be quantified spatially, as opposed to the percentage overlap. For aerial imagery Agisoft (2016b) suggests 80% forward overlap of images in a single flight line and 60% side overlap for adjacent flight lines. This corresponds to a maximum of 15 overlapping images when the camera orientation for all images is straight down. In our study, many locations were captured by more than 15 overlapping images because we took photographs from oblique angles.

Different combinations of the entire set of photographs were employed on Flumes 3 and 5 to test the effect of image orientation, number of images, and image overlap on SfM point cloud density and quality. The combinations included all images (All images) for both JPG and RAW, only images taken from the middle positions looking upstream and downstream (US-DS images), only images taken from the side of the flume (LB-RB images), only diagonal images taken from the side of the flume (LB-RB angled images; i.e., 45° and 135° images only), only images taken from the middle of the flume with 45° and 135° images from the side of the flume (no cross-flume images), all images from every second position, all images from every third position, and all images from every fourth position (Fig. 3b).

Photographs for the pan were collected using the same camera and lens as for the flumes. The pan filled with sediment was placed on a rotating turntable and the camera was positioned at six different distances (approximately 0.5, 0.75, 1, 1.5, 2, and 3 m) from the center of the pan to the camera sensor for two angles (30° and 60°) above horizontal (Fig. 3c). Images of the turntable were taken at 10° intervals, resulting in 36 images for each distance at each camera angle (Fig. 3d). Seven markers were placed on the turntable around the pan to aid in both image alignment and point cloud scaling/referencing.

2.3. SfM point cloud creation

Three-dimensional point clouds were created from each set of images using two different SfM software options: Agisoft PhotoScan Professional version 1.2.3 (Agisoft, 2016a) and VisualSfM version 0.5 (Wu, 2013; Wu et al., 2011). PhotoScan is widely used proprietary software that allows the user to select the level of alignment accuracy and dense cloud quality. VisualSfM (VSFM) is freely available from <http://ccwu.me/vsfm/> and implements a scale invariant

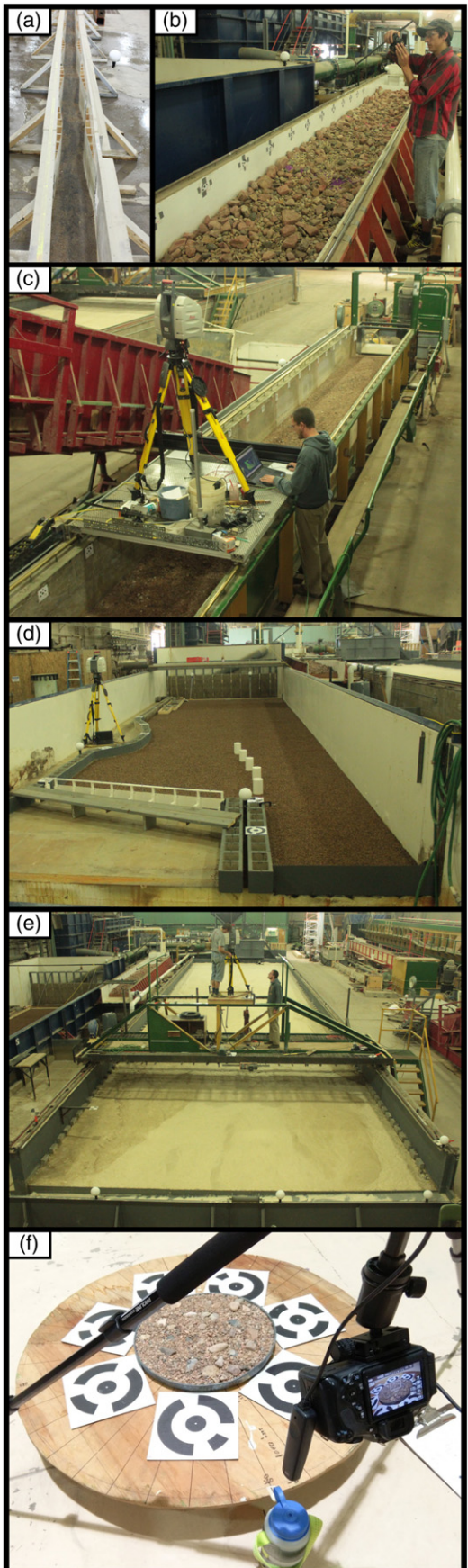


Fig. 1. Photographs showing the setup and grain sizes for (a) Flume 1, (b) Flume 2, (c) Flume 3, (d) Flume 4, (e) Flume 5, and (f) the pan.

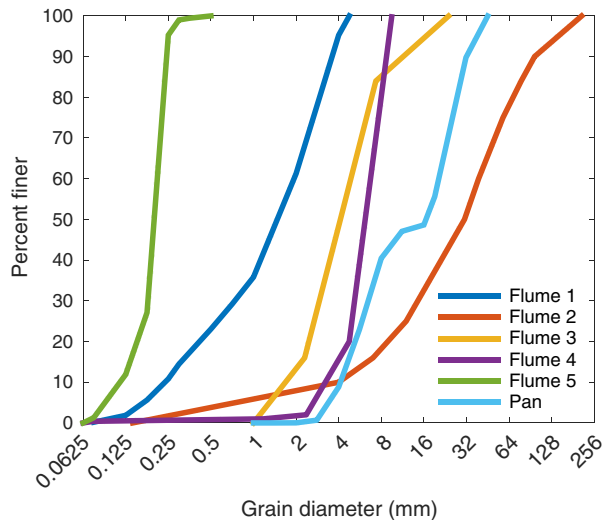


Fig. 2. Surface grain size distributions present in each flume.

feature transform (SIFT) (Lowe, 2004) and multi-core bundle adjustment (Wu et al., 2011) to recreate a three-dimensional scene from the two-dimensional images (Wu, 2013). The software also has the ability to integrate the Clustering Views for Multi-view Stereo/Patch-based Multi-view Stereo version 2 (CMVS/PMVS2) tool developed by Furukawa and Ponce (2010) to create a denser point cloud.

Comparisons between SfM and TLS elevation datasets used SfM point clouds generated from all of the images acquired in each flume. The SfM datasets generated in PhotoScan used a photographic alignment accuracy set to “highest” (out of the options “lowest”, “low”, “medium”, “high”, and “highest”) and a dense cloud quality set to “medium” (out of the options “lowest”, “low”, “medium”, “high”, and “ultra high”). Although PhotoScan has the ability to specify targets or ground control points to aid in image matching, no targets were specified for the objective of testing these different settings. Although some process settings can be specified by the user in VSFM, only default settings were used for this study.

In order to explore the effect of the user-controlled settings in PhotoScan on the final point cloud density and quality, we processed the photos taken of Flume 3 in a variety of ways and compared the results. We varied the alignment accuracy setting from “lowest” to “medium” to “highest” and we varied the dense cloud quality setting from “lowest” to “medium” to “ultra high”. Additionally, we tested the effect of selecting targets in the software processing for three of the image combinations: all images, US-DS images, and LB-RB images. Printable targets were obtained through PhotoScan software. For Flumes 2 and 3 targets had previously been taped to the inside of the flume walls at a spacing of approximately 0.5 m in the downstream direction. For Flumes 1, 4, and 5, targets were spread out at the edges of the imaged area, either in or around the flumes.

Point clouds for the pan experiment were generated in PhotoScan using the “highest” alignment accuracy setting and the “ultra high” dense cloud quality setting.

2.4. Point cloud scaling and alignment

The free, open-source software CloudCompare (Girardeau-Montaut, 2011) was used to align and scale the SfM point clouds, and to align the Faro point clouds to the Leica point clouds. This process began by importing all the clouds for a given flume. Three readily identifiable points in common between each cloud (e.g., flume wall corners) were selected to initially align the reference cloud to the

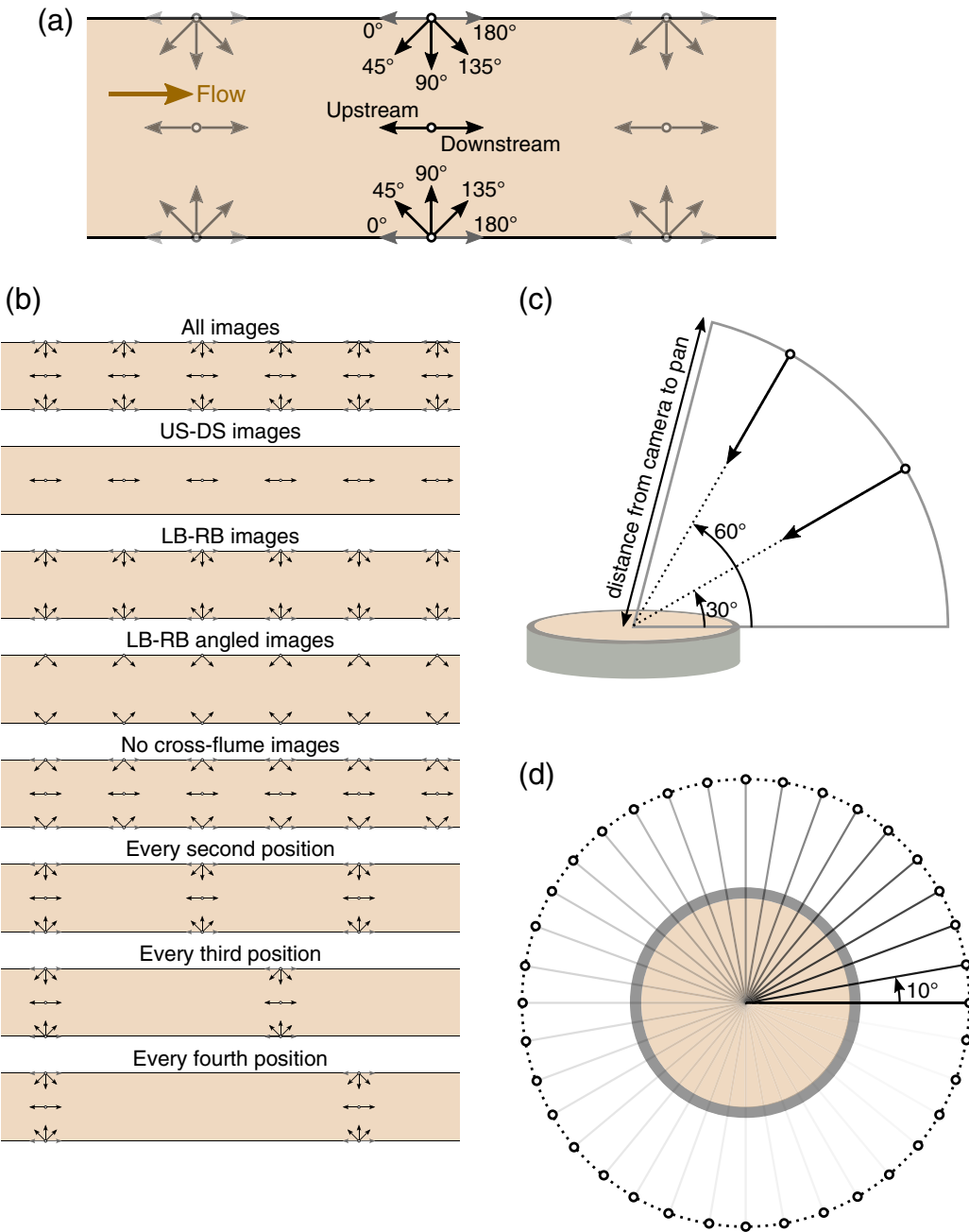


Fig. 3. Conceptual illustrations showing (a) the approximate camera angles for flume imagery, (b) the different combinations of images tested for Flumes 3 and 5, (c) the vertical angles for the pan imagery, and (d) the horizontal angles for the pan imagery.

Leica base cloud. These point clouds were all clipped to a rectangular box that eliminated points outside the flume, yet kept the walls. The iterative closest point (ICP, see Besl and McKay, 1992) algorithm was then used to finely register the two point clouds together by using a random sampling limit of 100,000 points and was reduced to a root mean square (RMS) difference between the point clouds of 1.0×10^{-5} m. The point clouds were then clipped such that walls and structures in the flume were removed.

The pan point clouds were aligned using measured arbitrary coordinates in the scene. Seven markers were placed around the pan and the coordinates of each of those targets were used in all the photo-to-scale and align each point cloud in PhotoScan. The point clouds were clipped to a circular area such that the rotating turntable and pan edges were removed.

2.5. Point cloud processing

In order to quantitatively compare the TLS and SfM methods, point cloud post-processing consisted of calculating statistics related to model elevations, two surface roughness metrics, and computation of the spatial differences between each point cloud. The first surface roughness calculation was a single value for rugosity, which was measured for the entire final, clipped point cloud for each flume. Rugosity is defined as the 3D surface area of a region divided by the planimetric, or 2D, surface area of the same region (Brasington et al., 2012). A triangulated irregular network (TIN) was created from each point cloud in ArcGIS and the 'Surface Volume' function in the 3D Analyst toolbox calculated the necessary areas. The second approach of estimating surface roughness was to use a spatially

Table 2

Point cloud sizes and times associated with acquisition for each method in each flume.

Flume	Image count	Approx. longitudinal image spacing (cm)	Cloud	Data acquisition time (h)	Point count	Avg. point density (points per cm ²)
1	388	20	Leica	1.8	119,105	9.3
			Faro	1.0	485,116	37.8
			PhotoScan	0.8	7,220,309	562.2
			VSFM		6,340,931	493.8
2	218	50	Leica	3.0	1,229,703	12.3
			Faro	1.0	4,021,050	40.5
			PhotoScan	0.7	14,767,625	148.6
			VSFM		14,919,139	150.1
3	266	60	Leica	2.5	619,293	3.3
			Faro	1.0	2,030,260	10.7
			PhotoScan	0.7	14,368,454	75.7
			VSFM		14,452,316	76.2
4	248	80	Leica	3.0	1,174,194	3.6
			Faro	1.0	2,598,663	8.0
			PhotoScan	0.8	6,313,620	19.4
			VSFM		8,603,440	26.5
5	429	100	Leica	2.8	3,076,640	1.7
			Faro	1.0	10,659,966	5.8
			PhotoScan	1.1	18,006,588	9.8
			VSFM		8,910,358	4.8

variable roughness index-elevation. This measure of roughness is computed as the standard deviation of residual topography across a moving window for a specified number of cells (e.g., Cavalli et al., 2008; Prosdocimi et al., 2015). For this calculation the point cloud data were first gridded onto a raster with 1 cm cells. Residual elevations were computed by differencing each cell's value in a 5 × 5 cell window with the mean value of those same 25 cells. The roughness index-elevation of the cell in the center of the window is defined as the standard deviation of those elevation residuals (see Cavalli et al., 2008, for more details). Ideally both the raster cell size and computation window size would vary according to point density, grain size, feature size, and noise (Prosdocimi et al., 2015). However, because we are mainly interested in the differences between methods, we used the same cell and window size for all five flumes and all four methods of point cloud creation. Roughness values may not be comparable between flumes because the number of grains present in the 5 × 5 cell window will depend on the grain-size distribution of the sediment in each flume.

Point cloud differencing was computed using the Multiscale Model to Model Cloud Comparison (M3C2) algorithm (Lague et al., 2013). This differencing method is available in CloudCompare and requires the user to define several parameters. The general concept behind M3C2 is to compute cloud-to-cloud distances using a local normal direction rather than only the vertical direction. The normal direction is computed from the points within a sphere around a given point, defined by the so-called "normals diameter". Once the normal direction is computed, the algorithm creates a cylinder oriented along the normal vector, with a diameter (the "projection diameter") specified by the user. The intersection of each point cloud with this cylinder defines two subsets, which are projected on to the axes of the cylinder and used to compute a distribution of normal distances between the two clouds at that location. More details on the M3C2 algorithm are provided by Lague et al. (2013).

For the purpose of our study we chose to always specify the point cloud with fewer points as the reference cloud, and also chose to use the entire reference point cloud to be the core points for which M3C2 differences were computed. A sensitivity analysis on the mean, median and standard deviation of the M3C2 differences for Flume 3 were relatively insensitive to adjusting the normal and projection diameters. We ultimately chose to use normal and projection diameters of 5 cm and 1 cm, respectively, for all of the flumes. Lague et al. (2013) suggest that these values should vary relative to local point cloud roughness, however for simplicity and consistency we

elected to use the same values for all flumes and point clouds. Unlike many previous SfM validation studies which compared SfM models to other models by first converting one or both point clouds to rasters (Smith et al., 2015), the M3C2 algorithm allowed us to compare point clouds directly. M3C2 differences were computed for all point cloud combinations.

Considering the accuracy of the TLS units and the fine level of detail in the imagery and subsequent SfM point clouds for the sediment in the pan experiment, no TLS data were collected. Instead, the different SfM point clouds were qualitatively evaluated against one another to determine whether individual grains were discernible and at what distance the differences between individual grains was smoothed over.

3. Results

3.1. TLS and SfM comparisons

3.1.1. Point density and image overlap

The horizontal spacing between photographs was varied between flumes due to their varied sizes (Table 2), which resulted in substantial photo overlap across most of the flume for all flumes (Figs. 4a–8a). Larger flumes contain areas with greatest image overlap and the greatest overlap generally occurs near the center of the flume just downstream from the middle. For each flume the point count and point density vary over an order of magnitude (Table 2). In every case the Leica model contains the fewest number of points. The TLS models nearly always have lower point counts than the SfM models, with the exception of Flume 5, where the Faro model contains more points than the VSFM model. Spatial distributions of the point density results for the TLS models in each flume illustrate a strong dependency on the location of the TLS scanner (Figs. 4b–8b), where overlapping scans had one or more orders of magnitude more points than areas that were only included in a single scan. The point density map of the VSFM model of Flume 5 shows large gaps where no point data exists (Fig. 8b).

3.1.2. Bed elevations and roughness metrics

Elevation values for each method are generally similar for each flume (Figs. 4c–8c); however, the range of elevation values for the VSFM model in Flume 4 is greater than the other clouds (Table 3). Both rugosity and the roughness index-elevation calculations were derived from elevation values (Table 3). Rugosity is greatest for

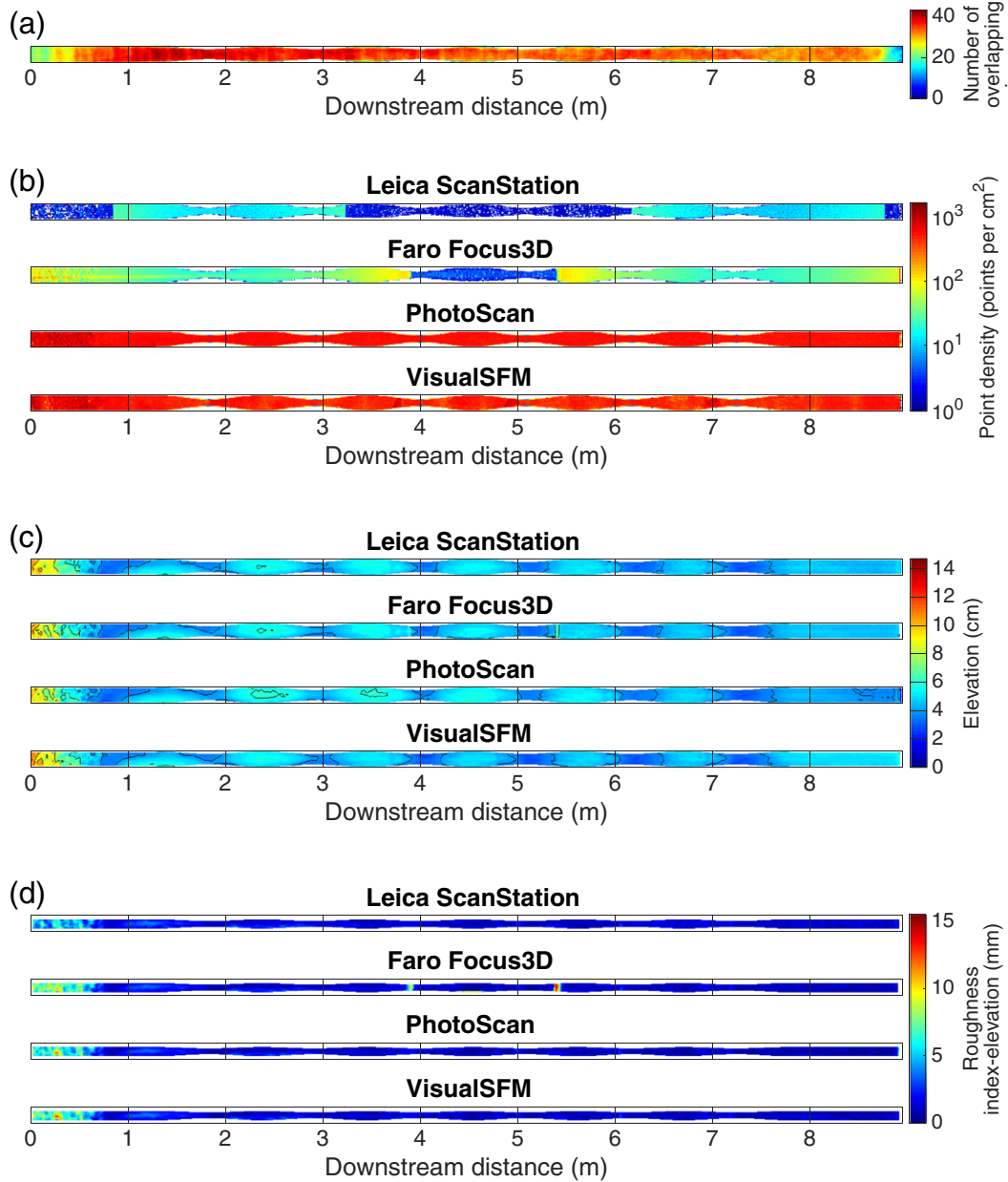


Fig. 4. Flume 1 maps showing (a) image overlap count for all images collected for SfM and (b) point density, (c) elevation, and (d) roughness index-elevation for Leica ScanStation, Faro Focus3D, PhotoScan and VisualSfM models.

Flume 2 where the D_{50} is 31.0 mm, and in Flume 4 the rugosity for the VSFM model is nearly four times that of the other models. The maps of the roughness for each flume illustrate both form and grain roughness features such as alternate bar edges in Flume 3 and individual grains in Flume 2 (Figs. 4d–8d). For each flume both rugosity and roughness index-elevation values are generally greatest for the VSFM models.

3.1.3. M3C2 differences

Differences computed using the M3C2 algorithm show that for most of the flumes 98% of the computed differences lie within 2 cm of each method (Fig. 9), with the exception of Flume 2 and some comparisons in Flume 5. Figs. S1 through S5 in the Supplemental Information show the spatial distribution of M3C2 differences for all model comparisons. Root mean square (RMS) values for the M3C2 differences are consistently at or under 1 cm for all flumes except

Flume 2. Comparisons between the two TLS models generally have the smallest range of M3C2 distance encompassing the middle 98%, with the exception of Flume 2. Comparisons between all of the models in Flume 3 are the most consistent with RMS values varying between 2 and 3 mm.

3.2. Image combinations

The spatial patterns of image overlap for the different photo acquisition protocols for Flume 3 are shown in Fig. 10. The smallest number of overlapping images for any area is four, which occurs for the image combination including only angled images taken from the side (LB-RB angled images). The greatest number of overlapping images, 51, occurs when all images are used. Despite the different amount of overlap between image combinations, there was little difference in the number of points in each point cloud for Flume 3

(Table 4). The combination using only images taken from the middle of the flume pointing in the upstream and downstream directions (US-DS images) was not able to align in PhotoScan without the selection of targets. Alignment was unable to be performed, with

or without targets specified, for image combinations using images acquired from every third and every fourth position. Computed M3C2 distances between each of the image combinations and select combinations with and without targets specified against the Leica model show relatively little difference (Fig. 11 and supplemental Fig. S6). Median and RMS values for these M3C2 differences show almost no variation between image combinations (Table 4).

Image overlap maps computed from different image combinations for Flume 5 are shown in Fig. 12. The maximum number of overlapping images for any point is 96 and occurs when all the images are used. The minimum is one, occurring for the LB-RB angled images. There is greater range in the point counts for different image combinations of Flume 5, with models created from RAW images, US-DS images, and every third position having about half the point count as the other image combinations (Table 5). Alignment was unable to be performed, with or without targets specified, for the image combination using images acquired from every fourth position. There is greater range in the M3C2 distances from the Leica model for point clouds of Flume 5 than Flume 3 (Fig. 13). The spatial distribution of these M3C2 distances are shown in supplemental Fig. S7. Median values for RAW images and every third position and RMS values for RAW images, RB-LB angled images, and every third position are greater than the other image combinations.

Although PhotoScan has the option of automatically detecting targets in the input images, we have not had luck with that feature. The placement of targets required the manual selection of the markers in each image in PhotoScan. For each photoset this took approximately 30 min.

3.3. PhotoScan settings

Calculated M3C2 distances between models of Flume 3 using the different qualitative settings for PhotoScan's processing of both image alignment accuracy and dense point cloud quality against the Leica model are summarized in Fig. 11, with the spatial distribution of these distances shown in supplemental Fig. S8. These results show a slight decrease in central 98% of M3C2 distances as the accuracy and quality settings are increased. However, the median and RMS values for the M3C2 distances between the SfM clouds and the Leica TLS cloud show very little variation between PhotoScan settings (Table 6). The primary differences between settings are in the point count for each model and the processing time, which for a typical desktop computer is roughly on the order of minutes for lowest quality, hours for medium quality and days for ultra high quality. The dense cloud quality setting has a much larger effect on point density than image alignment accuracy, where total point counts between dense cloud qualities of "lowest", "medium", and "ultra high" vary by over an order of magnitude each (Table 6). Therefore, the "quality" setting in creating dense clouds is analogous to density.

3.4. Camera distance and angle

A summary of point counts for the point clouds generated in the pan experiment is shown in Table 7. The difference in point count is much more pronounced between the different distances than between the two different angles. There is a general power-law decay in model point count with increased distance between the camera and subject (exponent of approximately -2.15). Although the point clouds generated from 30° imagery tended to have a higher point count than those generated from 60° imagery the differences are minor. Figs. 14 and 15 show selected cross-section profiles of the created point clouds through the center of the circular pan (an animation showing cross-section profiles for every 1° of rotation is available with the supplemental material). Both the clouds from 30° images and 60° images show a "smoothing" with increased distance

Fig. 5. Flume 2 maps showing (a) image overlap count for all images collected for SfM and (b) point density, (c) elevation, and (d) roughness index-elevation for Leica ScanStation, Faro Focus3D, PhotoScan and VisualSfM models.

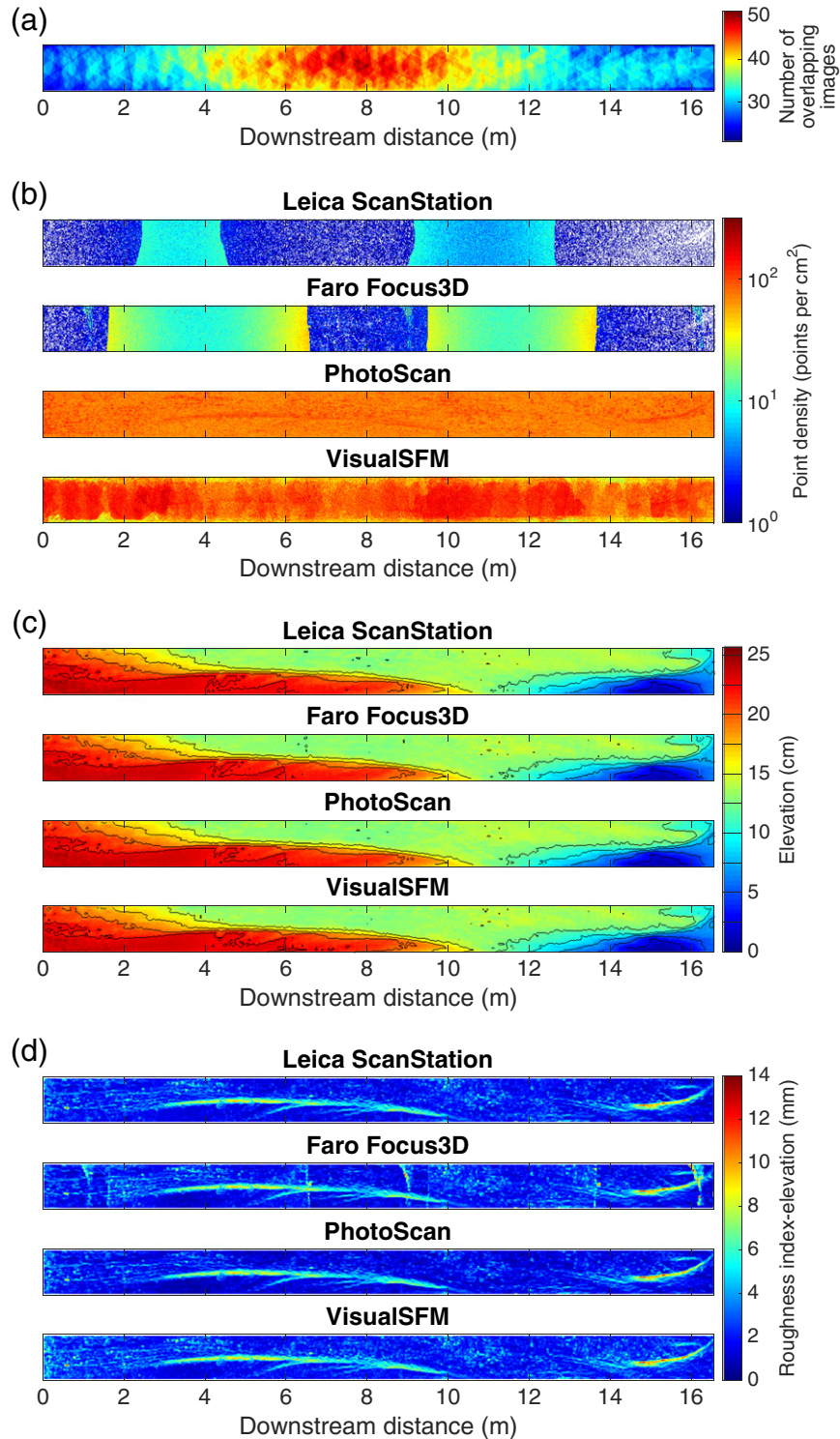


Fig. 6. Flume 3 maps showing (a) image overlap count for all images collected for SfM and (b) point density, (c) elevation, and (d) roughness index-elevation for Leica ScanStation, Faro Focus3D, PhotoScan and VisualSfM models.

between the camera and the surface. For the models made from the closest imagery the interstices between individual grains are relatively clear. As the camera distance increases the difference between the “lows” separating grains and the “highs” at grain apices are reduced, especially for the smaller grains (e.g., those at the right of the plots in Fig. 15).

4. Discussion

4.1. TLS and SfM comparisons

The image count for each flume is mostly a function of flume dimensions and the camera height above the flume bed. In general

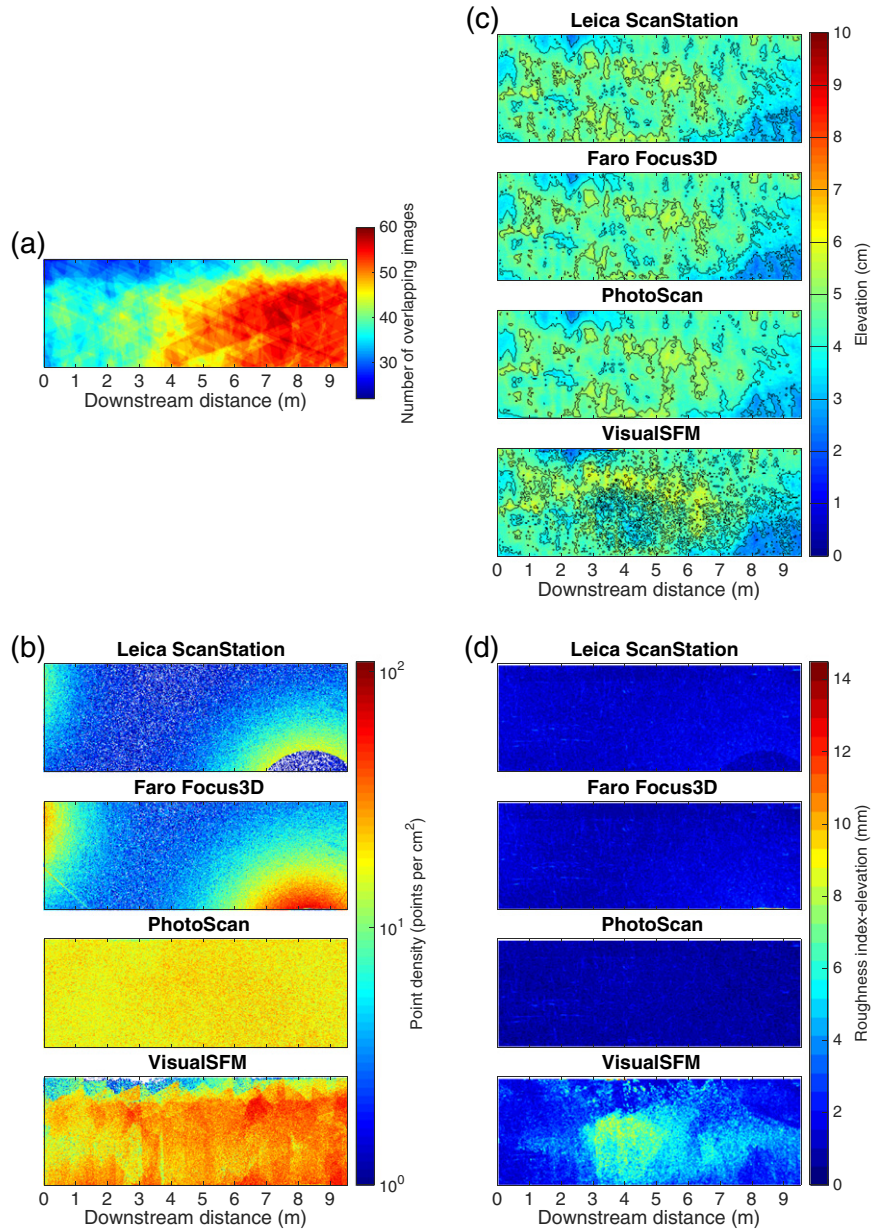


Fig. 7. Flume 4 maps showing (a) image overlap count for all images collected for SfM and (b) point density, (c) elevation, and (d) roughness index-elevation for Leica ScanStation, Faro Focus3D, PhotoScan and VisualSfM models.

the maximum image overlap increases with increasing flume size. Flumes 2 and 5 each have a concentration of high image overlap slightly downstream from the middle of the flume, which can be explained by the slope of the flume bed, i.e., camera positions looking in the downstream direction are able to see a greater area of the flume bed because the bed is sloping away from the camera's viewpoint. Flume 3 also appears to have an area of high image overlap slightly downstream from the middle, however, it should be noted that the data shown in Fig. 7 are clipped and do not represent the total area of the flume. The suggestion of Agisoft (2016b) for 80% forward overlap of images in a single flight line and 60% side overlap for adjacent flight lines corresponds to a maximum image overlap count of 15, generally well below what we achieved with our image overlap.

Processing time for both the TLS and SfM methods are highly dependent on the size of the dataset, computer power, and the user familiarity with the software. We did not include processing time

for each method as we used multiple computers, each with different processors and available RAM. Raw data acquisition time was generally lower for the SfM imagery than the TLS scans, with the single exception of the Faro in Flume 5. To obtain data of similar point densities with manual measurements would take an extremely long time. Even more modern, conventional methods of measuring flume topography could potentially be very time consuming. Lane et al. (2001) reported an acquisition time of 8 h to obtain data necessary to create a DEM with 0.5 mm resolution on a 0.25 m × 0.25 m area, using a laser sensor on a motorized cart. The SfM imagery for each of the smaller flumes was collected in less than an hour and produced point clouds with multiple points per mm^2 (Table 2). By adjusting the software settings the point density has the potential to increase dramatically (Table 6). In the pan experiment imagery for each phototest required mere minutes to collect and resulted in a coverage area nearly twice that used by Lane et al. (2001) and at a minimum of several points per mm^2 .

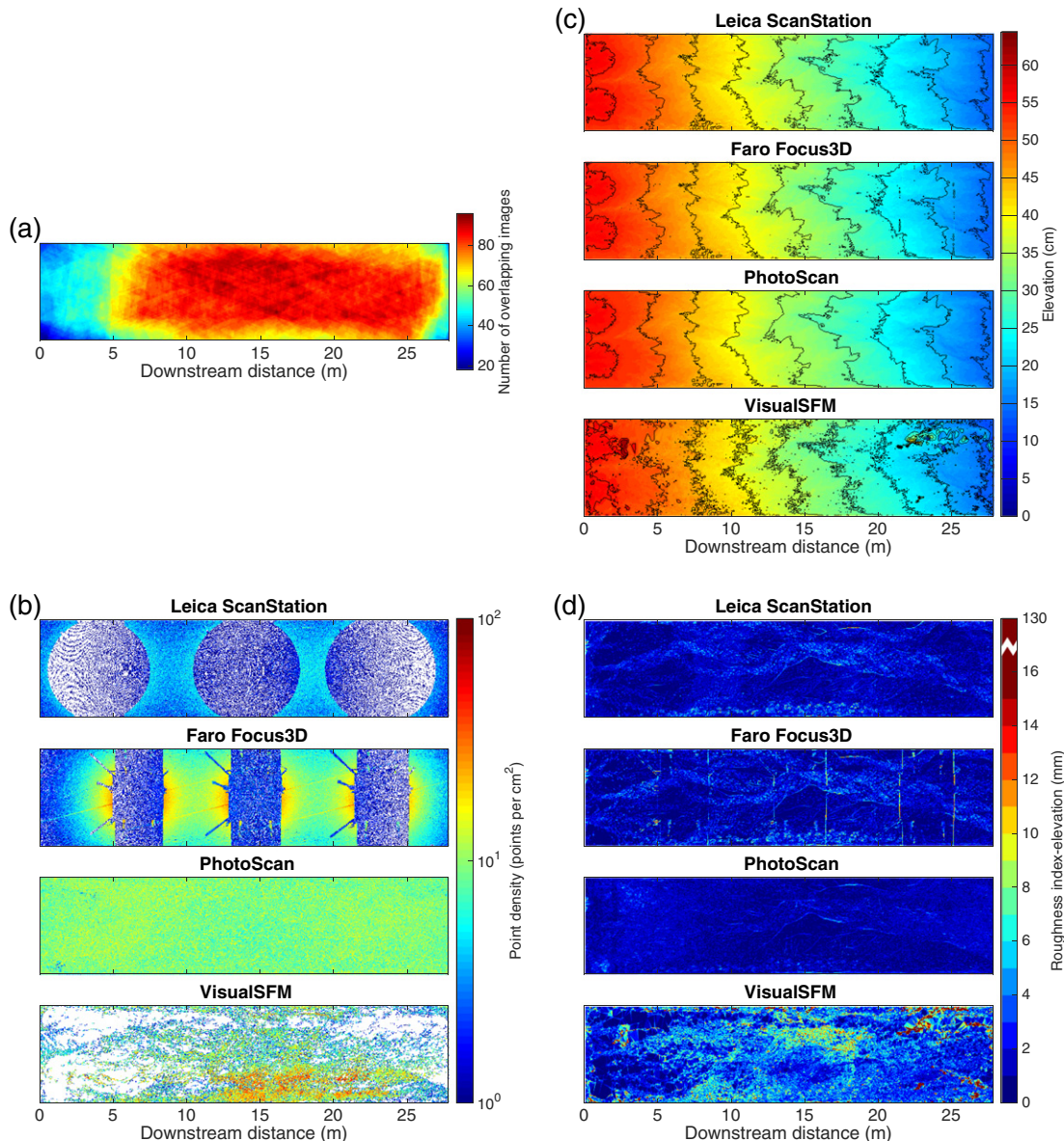


Fig. 8. Flume 5 maps showing (a) image overlap count for all images collected for SfM and (b) point density, (c) elevation, and (d) roughness index-elevation for Leica ScanStation, Faro Focus3D, PhotoScan and VisualSfM models.

The point counts and spatial point densities of the topographic models show a high dependence on the method used to collect the data. The lower point count and density associated with the TLS models is due largely to both the limited number of scanning positions and the settings of each scanner. Had more scans been performed from additional stations or scanner resolution increased the point counts would have been higher, but at the cost of additional acquisition and processing time. Lower point density in areas of less image overlap would seem logical, however it came as a surprise that PhotoScan models show a spatially consistent point density for each flume. The VSFM models, on the other hand, show spatial point density distributions with generally lower values near the flume walls. The average point densities between the two SfM models are comparable to one another with the exception of Flume 5, where PhotoScan produces a model with twice the density of VSFM. Based on the spatial distribution of points in the VSFM model we suspect that the software had a difficult time with the apparent lack of texture and color of the fine sand surface. PhotoScan, however,

continued to produce a spatially consistent point cloud, even in areas with little texture. Given the proprietary nature of the algorithms in PhotoScan, it is difficult to know for certain the reason it produces more consistent point densities.

In general the elevation values and ranges for the different methods are comparable to one another. The VSFM model for Flume 4, however, has an elevation range two to three times larger than the other models (Table 2). This high elevation variability is obvious in the elevation map and propagates to produce higher ranges in roughness (Fig. 7). With the similarity in grain sizes between Flumes 3 and 4, this wider range of elevations in the VSFM model for Flume 4 can likely be attributed to two factors. First, as a result of the greater flume width/height the camera positions for Flume 4 were located a greater distance from the bed than the camera positions for Flume 3. Smith and Vericat (2015) report from more than 15 validation studies that the root mean square error of SfM models increases linearly with the range of imagery from the subject. However, the range scales reported there cover three orders of magnitude, which is much

Table 3

Point cloud elevation and roughness values for each method in each flume.

Flume	Cloud	Elevation (cm)		Rugosity	Roughness index-elevation (cm)		
		Range	Std. dev.		Range	Median	Std. dev.
1	Leica	9.4	0.8	1.42	0.8	0.1	0.1
	Faro	17.4	1.5	1.61	1.5	0.1	0.2
	PhotoScan	11.8	1.2	1.26	1.2	0.1	0.1
	VSFM	10.7	1.4	1.62	1.3	0.1	0.2
2	Leica	43.3	6.4	4.11	7.3	1.0	0.6
	Faro	52.1	8.3	6.09	7.1	1.1	0.7
	PhotoScan	46.2	7.2	5.73	6.9	1.0	0.7
	VSFM	51.4	6.6	6.77	11.1	1.2	0.7
3	Leica	25.7	4.2	1.19	1.1	0.2	0.1
	Faro	25.6	4.3	1.27	1.3	0.2	0.2
	PhotoScan	25.5	5.1	1.12	1.2	0.2	0.1
	VSFM	26.6	5.0	1.97	1.3	0.2	0.1
4	Leica	4.7	0.7	1.16	0.4	0.1	0.0
	Faro	7.0	0.8	1.15	0.4	0.1	0.0
	PhotoScan	4.2	0.6	1.06	0.4	0.1	0.0
	VSFM	14.6	0.9	4.22	1.4	0.3	0.2
5	Leica	51.5	11.1	1.08	1.6	0.1	0.1
	Faro	52.4	11.2	1.09	3.0	0.1	0.1
	PhotoScan	53.2	12.3	1.14	9.7	0.1	0.1
	VSFM	64.5	9.0	1.78	12.6	0.3	0.4

more variation than what we have between Flumes 3 and 4. Still, the closer camera angles for Flume 3 are more likely to produce more consistent feature matches of individual grains in the images, while single grain features may be difficult to match in Flume 4. Second, the wider range of elevations in the VSFM model of Flume 4 may be due to a relative lack of image texture. Flume 3 had both a wider range of grain sizes as well as grains of different colors, while the grains in Flume 4 were of more uniform size and color. This may have produced difficulty in feature detection and matching that was exacerbated by the dark color of the sediment and relatively low lighting. It is curious, however, that such elevation variability was produced in the VSFM model but not the PhotoScan model. Again, without knowledge of PhotoScan algorithms it is difficult to interpret the different results from the two SfM software packages. A lack of image texture also likely contributed to the elevation variability in the VSFM model of Flume 5 (Fig. 8).

Similar to the elevation results, rugosity and roughness index-elevation calculations are comparable for each model. Smaller grain sizes and topographic relief (e.g., Flume 5) result in much lower roughness parameters than larger grain sizes (e.g., Flume 2) and more significant relative topographic relief (e.g., Flume 1) (Table 3). As mentioned previously, the “noise” in some of the elevation values can propagate to create variability in the roughness metrics. It should be remembered that we used the same moving window and cell size for roughness index-elevation calculations regardless of grain size. For most of the flumes both elevation and roughness calculation are comparable between the TLS and SfM models despite large differences in point densities.

The M3C2 distances show a high degree of variability across flumes, and among models (Fig. 9). The widest range of M3C2 distances occurs for the models of Flume 2, and this is primarily due to “shadows” in the TLS models, resulting in limited coverage between

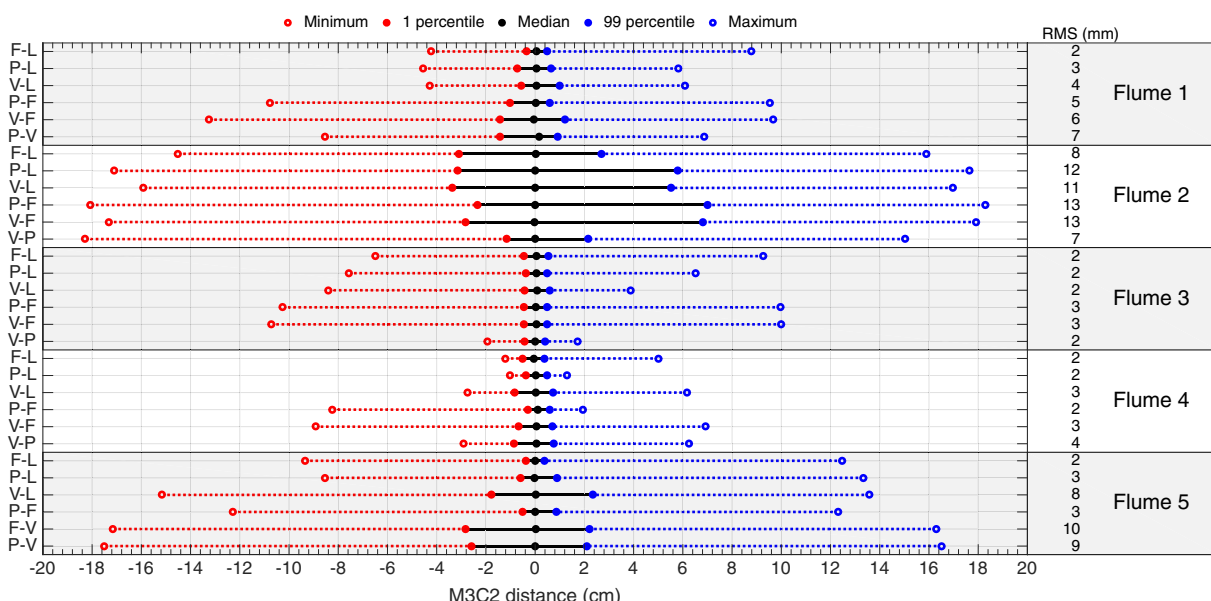


Fig. 9. Minimum, 1 percentile, median, 99 percentile, and maximum for M3C2 differences between each combination of models for each flume, such that the black line encompasses 98% of the measured M3C2 distances. L=Leica, F=Faro, P=PhotoScan, and V=VisualSfM.

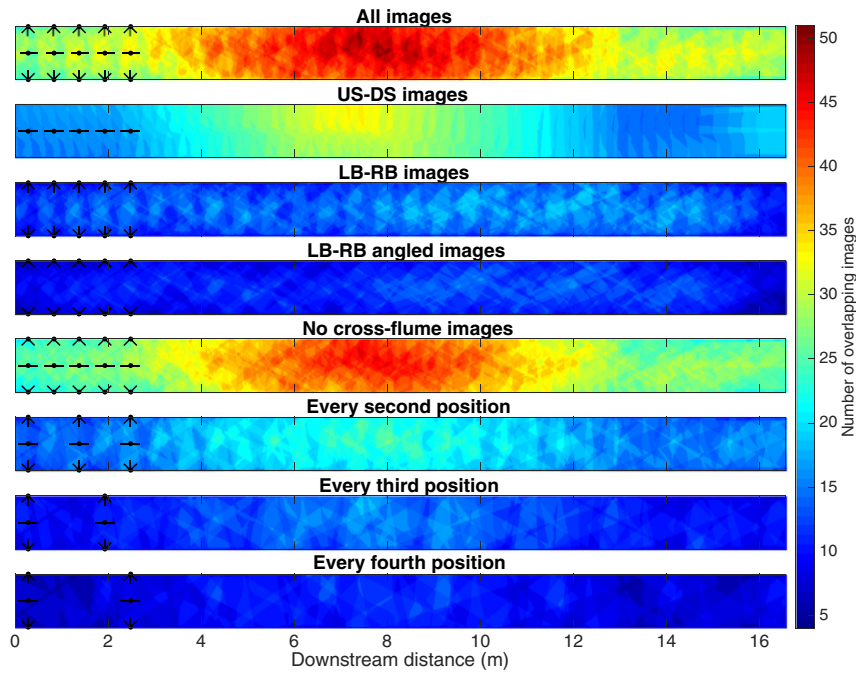


Fig. 10. Flume 3 maps showing the count of overlapping images for each of the image combinations. Note that camera positions and directions indicated by the black dots and lines are for illustrative purposes only and do not represent actual image positions and angles.

grains. In contrast the SfM approaches were more capable of creating detailed topography between grains due to the hundreds more locations from which photos were taken, as compared to the three instrument points used in the TLS data acquisition. An additional source of discrepancy could stem from error in the computed normal directions in the M3C2 algorithm, which would result in greater M3C2 distances between point clouds. It has also been pointed out that rough surfaces result in increased error effects (Prosdocimi et al., 2015). Computed distances between models mostly fall within ± 2 cm for Flumes 1, 4 and 5, and more than 98% of the measured distances are within ± 1 cm for Flume 3. M3C2 distances for Flume 2 reach upwards of 7 cm as a result of the higher roughness. In most cases the distances between the two TLS models is the lowest, and the distances between the TLS and SfM models fall within the reported error range of the TLS instruments.

The spatial distribution of M3C2 distances does not appear to show any patterns except for in Flume 1 where there is obvious nonlinear longitudinal deformation in the SfM models (Fig. 16). Because of the deep and narrow dimensions of Flume 1 the differences in camera angles are minute and result in more-or-less parallel imagery. James and Robson (2012) note that SfM analyses generally

rely on angles that are convergent rather than parallel, and parallel imagery in other close-range photogrammetry applications has been shown to result in lens model errors propagating and expounding in the 3D model to produce a “dome” effect (e.g., Wackrow and Chandler, 2008, 2011). Interestingly, the direction of deformation of the PhotoScan and VSFM models are reversed from one another, highlighting another apparent difference in algorithms. It should be noted, however, that the measured magnitude of the doming effect in the SfM Models for Flume 1 is approximate to the range of accurate measurements for the TLS machines (Leica, 2016; Faro, 2011). The other flumes had sufficient convergence of images to avoid noticeable nonlinear deformation, demonstrating the importance of including convergent imagery during acquisition.

4.2. Image combination and PhotoScan setting comparisons

Understandably the number of overlapping images depends on both the number of camera positions and camera orientation (Figs. 10 and 12). The fact that the US-DS image combination for Flume 3 contains nearly the same number of images as the every third position combination (Table 4) yet has image overlap 4–6 times

Table 4
Image combinations comparison for Flume 3.

Image combination	Targets	Image count	Point count	M3C2 distances from Leica (m)	
				Median	RMS
All images (JPG)	No	266	14,368,454	0.001	0.002
All images (RAW)	No	266	14,091,686	0.001	0.002
All images (JPEG)	Yes	266	14,353,849	0.001	0.002
US-DS images	Yes	89	11,307,633	0.000	0.002
RB-LB images	No	177	14,231,567	0.001	0.002
RB-LB images	Yes	177	14,263,685	0.001	0.002
RB-LB angled	No	117	12,278,775	0.001	0.002
No cross flume	No	206	12,939,702	0.000	0.002
Every second	No	135	13,862,586	0.001	0.002
Every third	No	90	—	—	—
Every fourth	No	71	—	—	—

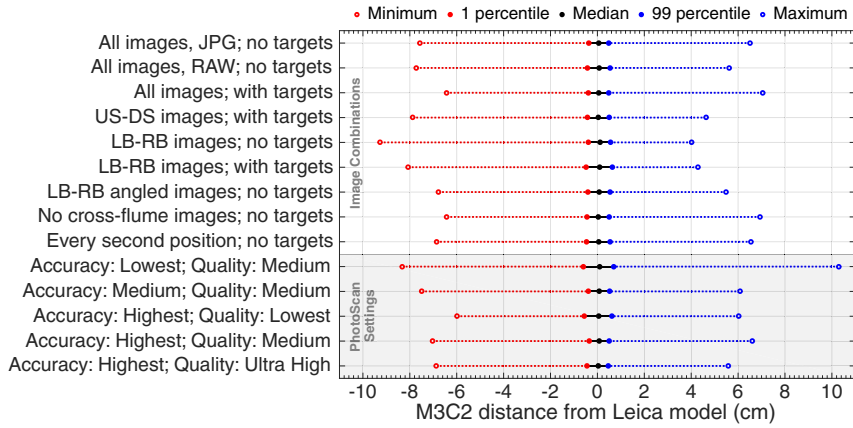


Fig. 11. Minimum, 1 percentile, median, 99 percentile, and maximum for M3C2 differences between SfM models created using different image combinations and PhotoScan settings for Flume 3, such that the black line encompasses 98% of the measured M3C2 distances.

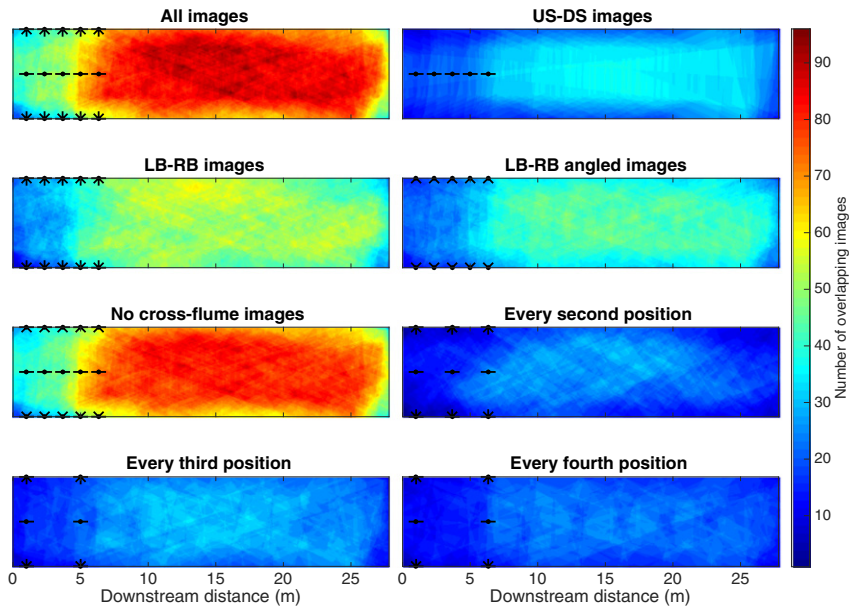


Fig. 12. Flume 5 maps showing the count of overlapping images for each of the image combinations. Note that camera positions and directions indicated by the black dots and lines are for illustrative purposes only and do not represent actual image positions and angles.

higher (Fig. 10) illustrates the importance of image orientation on achieving overlap. Similarly, the fact that the US-DS images were able to be aligned for Flume 3 while every third position could not be aligned further implies the importance of overlap rather

than number of images alone. For Flume 3 the corresponding point counts for the models produced from different image combinations somewhat follow the image count, but the differences are minor. For Flume 5 the point counts do not seem to follow any pattern.

Table 5
Image combinations comparison for Flume 5.

Image combination	Targets	Image count	Point count	M3C2 distances from Leica (m)	
				Median	RMS
All images (JPG)	No	429	18,006,588	0.000	0.003
All images (RAW)	No	429	9,199,483	0.004	0.015
All images (JPG)	Yes	429	20,163,866	0.000	0.004
US-DS images	Yes	94	8,544,152	-0.001	0.004
RB-LB images	No	335	22,732,148	0.000	0.003
RB-LB images	Yes	335	24,198,759	0.000	0.003
RB-LB angled	No	134	19,155,313	0.000	0.009
No cross flume	No	362	19,425,883	0.000	0.004
Every second	No	223	14,776,760	0.000	0.004
Every third	No	146	8,597,343	0.006	0.024
Every fourth	No	114	—	—	—

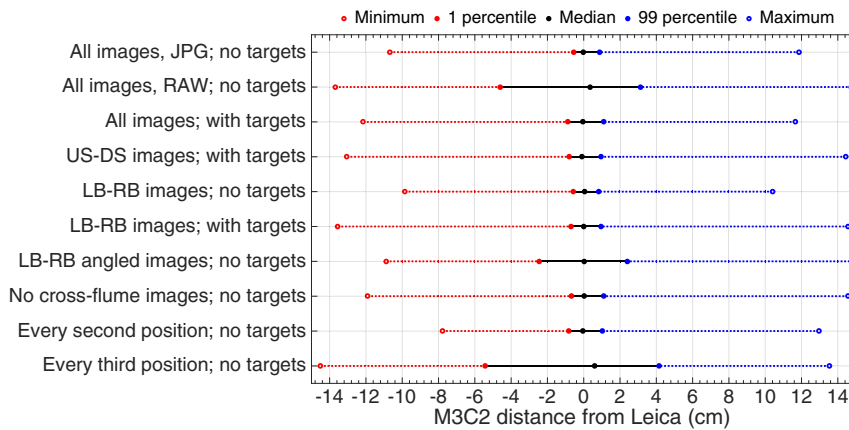


Fig. 13. Minimum, 1 percentile, median, 99 percentile, and maximum for M3C2 differences between SfM models created using different image combinations for Flume 5, such that the black line encompasses 98% of the measured M3C2 distances.

The fact that upstream and downstream oriented images taken from a position in the center of flume can only be aligned if targets are used is likely due to the extreme angle (180°) between the two orientations. The measured M3C2 differences of each image combination model against the Leica model for Flume 3 show very little deviation, suggesting that as long as PhotoScan is able to align images and create a 3D model the quality of point cloud is largely independent from both the number of images as well as the amount of image overlap (Fig. 11). We did not find any significant difference in using RAW imagery versus JPG files. However, in cases of over- or under-exposure and high lighting contrast, RAW images may have an advantage because their ability to retain more detailed color depth. Similarly, the selection of targets did not result in a significant change in M3C2 distances, however, the selection of targets is sometimes necessary for camera alignment to be successful, as seen in the case of the US-DS images. Target identification also provides a convenient method for scaling and aligning a point cloud, as would be necessary for a field application.

The primary difference between the variations in PhotoScan settings is the processing time required and the point count of the consequent model (Table 6), and even then only for the setting of dense construction quality. While the lowest alignment accuracy setting and the lowest dense quality setting produce a wider central

98% of M3C2 differences, it is still only on the order of millimeters and within the range of variability of the measurements themselves (Fig. 11). However, the model created using the lowest accuracy alignment shows a range of M3C2 differences 5–6 cm greater than the models created using other PhotoScan settings. Considering this, the selection of PhotoScan settings should be guided by particular applications and point cloud uses. For example, a dense quality set to “lowest” should probably only be used for qualitative assessment.

4.3. Camera distances and angles

In the results from our pan experiment, the differences are minute between the point clouds produced using SfM from images taken at different angles below horizontal and different distances between the camera and sediment surface (Figs. 14 and 15). In general the elevation differences in the cross-section profiles are no more than a millimeter or so. The major exception is in the interstices between some of the grains, where the closer camera locations show lower elevations (i.e., more pronounced differences between grains). In most cases the 0.5 and 0.75 m distance clouds fall very closely to one another, capturing the interstices between the fine particles, and the 2 and 3 m clouds fall closely to one another, smoothing over the interstices between the fine particles. Due to the higher angle

Table 6

Flume 3 point cloud summaries produced using different PhotoScan settings. Processing times should be taken as “order of magnitude” approximations for a standard desktop computer.

Accuracy	Quality	Point count	M3C2 distances from Leica (m)		
			Median	RMS	Processing time
Lowest	Medium	15,961,002	0.001	0.003	Hours
Medium	Medium	14,353,407	0.001	0.002	Hours
Highest	Lowest	794,090	0.001	0.003	Minutes
Highest	Medium	14,368,454	0.001	0.002	Hours
Highest	Ultra high	262,402,248	0.000	0.002	Days

Table 7

Point cloud sizes from pan experiment.

Distance (m)	30° imagery			60° imagery	
	Point count	Avg. pt density (pts per cm^2)		Point count	Avg. pt density (pts per mm^2)
0.5	32,824,726	282.0		29,562,203	25,390
0.75	15,417,582	132.4		15,200,162	13,060
1	7,831,331	67.3		8,127,557	6980
1.5	3,430,310	29.5		3,302,979	2840
2	1,844,637	15.9		1,706,091	1470
3	671,886	5.8		657,6620	570

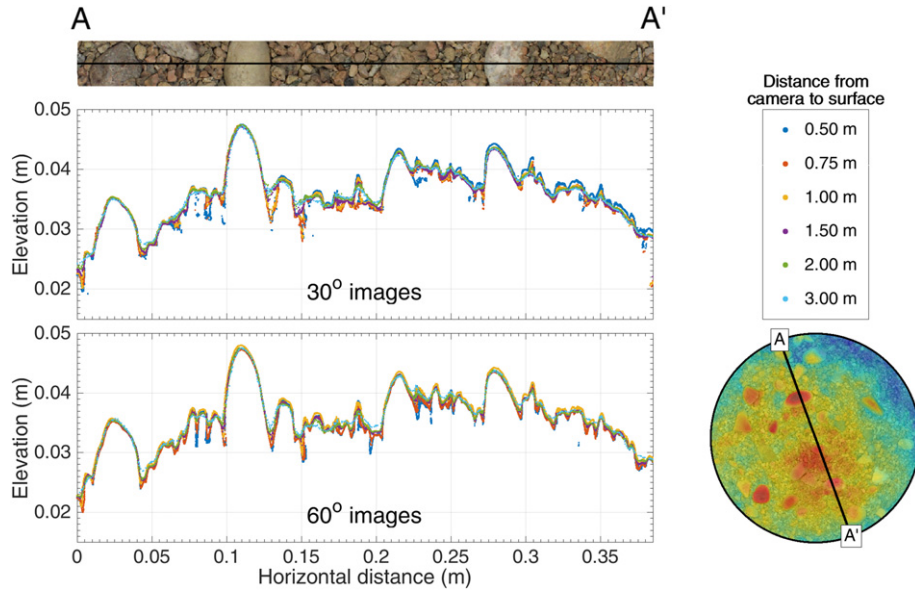


Fig. 14. Cross-section profiles at a rotation angle of -70° for the pan experiment. The top left image is from an orthoimage created in PhotoScan showing the line of the cross-section profile. The bottom right circle shows the entire area of interest for the pan with and the line of the cross-section profile. The profiles have a vertical exaggeration of 4.

and consequent ability to capture deep interstitial space between grains the 60° imagery seems to capture this void more readily and at greater distances than the 30° imagery. The 1 m imagery represents an apparent transition between photosets whose point clouds resolve the spaces between 2 mm particles and those that smooth over fine grain-scale detail. The Canon EOS Rebel T3i that was used to capture imagery has a megapixel (MP) count of 18 and with the 24 mm lens each image has approximately 2400 pixels across the pan diameter (0.385 m), resulting in a pixel spacing of equivalent to 6 pixels/mm with the camera located 1 m from the center of the pan. Because the imagery was taken from an oblique angle finer pixel spacing occurs closer to the camera (and conversely, coarser spacing farther). An unobstructed 2 mm grain (the smallest in the pan and assumed to be completely visible as a circle) would then occupy about 113 pixels (assuming the cross-sectional area of the grain is

about 3.14 mm^2), given the 6 pixels/mm (36 pixels/mm²) resolution at 1 m camera distance. From a camera distance of 1.5 m the average approximate pixels to 2 mm grain ratio decreases to 49. These findings suggest that SfM may be used to capture grain scale topography for particles occupying about 100 pixels, so the camera sensor resolution, lens focal length, and smallest resolvable grain-scale desired can be used to determine the distance.

4.4. Guidelines & recommendations for SfM in flumes

Our results suggest that SfM can produce topographic point clouds in flumes with quality comparable to TLS and much greater point density, with less acquisition time and at much lower overall cost. However, SfM may not perform as optimally for deep and narrow flumes, such as Flume 1, where it is difficult to obtain images

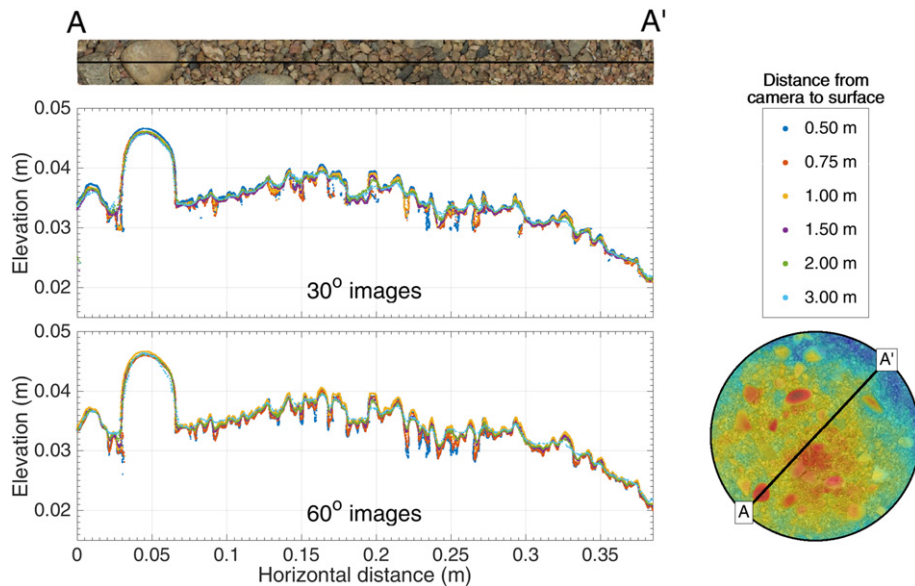


Fig. 15. Cross-section profiles at a rotation angle of 47° for the pan experiment. The top left image is from an orthoimage created in PhotoScan showing the line of the cross-section profile. The bottom right circle shows the entire area of interest for the pan with and the line of the cross-section profile. The profiles have a vertical exaggeration of 4.

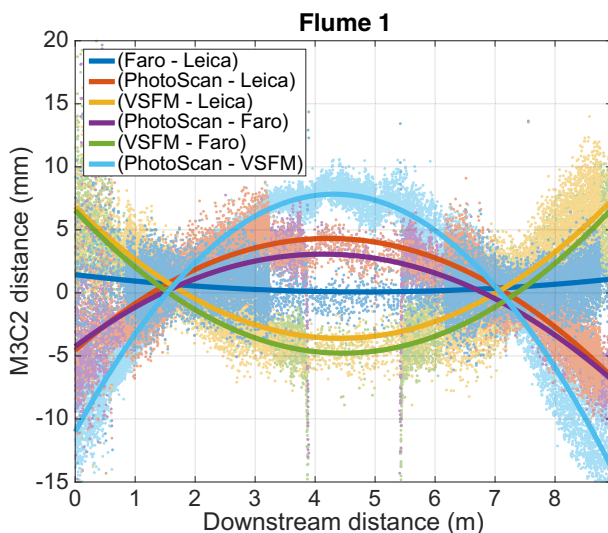


Fig. 16. Longitudinal M3C2 differences and fitted second-degree polynomials showing nonlinear deformation in the downstream direction of SfM point clouds for Flume 1.

from sufficiently convergent angles to completely alleviate lens distortion issues. Also, SfM requires image texture to define features and in cases of very small grains with camera positions a significant distance from the flume bed, as in Flume 5, some SfM algorithms may have difficulty in defining and matching features. Sediment of nearly all the same size and color under low light, as in the case of Flume 4, can also produce poor feature detection and matching. In these cases we would recommend additional ground control points on the flume surface and/or supplementary light sources to potentially increase image texture. However, care should be taken to ensure light sources are outside the field of view of the imagery and the camera flash should not be used (Agisoft, 2016b).

For image acquisition, we simply recommend that images are taken at a number of positions and angles that provide sufficient coverage of the flume bed. Agisoft's (2016b) recommendations of overlap of 80% in the downstream and 60% in the cross-stream directions result in an image overlap count of 15 and this seems like a reasonable goal. Insufficient overlap, which seemed to be the case when we skipped every third or fourth position in Flume 3, can make photo alignment impossible or significantly reduce the quality of the resultant model. If the differences between camera angles are too great it may be necessary to specify targets for the camera alignment. In our image combinations for both Flumes 3 and 5 the upstream and downstream facing camera angles from the center of the flume provided an acceptable output model with the fewest number of images. In general we found no significant difference in RAW imagery versus JPG, but for situations of under- or over-exposure we expect that RAW images may produce more satisfactory results.

PhotoScan consistently produced more satisfactory results than VisualSfM, particularly for point density. When selecting PhotoScan settings we recommend the default settings in version 1.2.3.2016 with the photo alignment accuracy set to "highest" and the dense cloud quality set to "medium". For cases where very high point density is required it may be necessary to increase the dense cloud quality, however it should be noted that this significantly increases the processing time.

The camera distance from the subject will depend greatly on the detail required as well as the sensor resolution and focal length. If sub-grain scale topography is required, we suggest positioning the camera a distance from the flume bed such that 100 pixels per grain is achieved. In our experiment the imagery captured from a steeper

angle above the horizontal seemed to result in a point cloud that characterized the interstices between grains more clearly, especially at farther distances. However, for cases of very poorly sorted sediment, for which there is little to no interstitial space, the angle of the camera would likely have less of an effect.

5. Conclusions

The lack of previous work involving Structure-from-Motion photogrammetry methodology in laboratory flumes has led us to conduct a series of experiments to explore how flume size, sediment size, photo acquisition, and software processing affects the density and accuracy point clouds derived using SfM photogrammetry. TLS and photographs were collected for five laboratory flumes, for which the resulting topographic models were compared, and photographs were collected at varying angles and distances from a pan of sediment to assess the ability to accurately characterize grain scale topography.

Both PhotoScan and VisualSfM tended to have comparable elevation accuracy, but PhotoScan generally produced more uniformly high point density than VisualSfM, and VisualSfM produced noisier topographic data for flumes of large size, low relief, and uniform grain size. Comparisons between different combinations of images show that the number of images, camera orientation, and number of overlapping images have little bearing on the character of the resultant point cloud model, either in total point count or in M3C2 distance from the Leica TLS model. Process settings in the PhotoScan software also showed to have negligible effect on the distance from the Leica TLS model. However, the dense quality setting did have a significant effect on the total point count in the resultant model and the processing time. The pan experiment showed that fine-scale detail decreased with increased distance between the camera and the subject. Point count was shown to decrease with distance as a power function to the -2.15 . Imagery taken at a steeper angle also produced more defined boundaries between grains. We suggest that the finest grain-scale topography likely to be resolvable using SfM photogrammetry methods will correspond to grains occupying about 100 pixels in the digital imagery.

These results ultimately indicate that SfM photogrammetry provides a viable alternative to other topographic measurement techniques, with the ability to provide higher resolution datasets of comparable quality, at a fraction of the cost and time. Additionally, the SfM photogrammetry software proved to be more intuitive and present less of a learning curve than TLS processing software. Given these considerations we expect SfM photogrammetry to continue gaining popularity in flume experiments, as well as other physical sciences.

Acknowledgments

We would like to acknowledge Andy Bankert and Dr. Lina Polvi for providing grain size distributions for Flumes 2 and 3, respectively. We also thank Dylan Armstrong for providing grain size distributions for Flumes 4 and 5, and helping with the processing of Leica data in Cyclone. J.A. Morgan and D.J. Brogan are supported by National Science Foundation grant EAR-1425067 and USDA National Institute of Food and Agriculture Hatch project 1003276, respectively. We would also like to thank three anonymous reviewers whose constructive comments helped clarify our manuscript.

Appendix A. Supplementary data

Supplementary data associated with this article can be found in the online version, at <http://dx.doi.org/10.1016/j.geomorph.2016.10.021>.

References

- Aberle, J., Nikora, V., 2006. Statistical properties of armored gravel bed surfaces. *Water Resour. Res.* 42, <http://dx.doi.org/10.1029/2005WR004674>.
- Agisoft, 2016a. Agisoft PhotoScan Professional Edition, version 1.2.3.2016. (Accessed 30 January 2016). <http://www.agisoft.ru/products/photoscan/>.
- Agisoft, 2016b. Agisoft PhotoScan User Manual, Professional Edition, version 1.2. (Accessed 30 January 2016). http://www.agisoft.com/pdf/photoscan-pro_1_2_en.pdf.
- Autodesk, 2016. . Accessed 19 September 2016 Autodesk ReMake: high definition 3D from reality. <https://remake.autodesk.com/about>.
- Bertin, S., Friedrich, H., Delmas, P., Chan, E., Gimelfarb, G., 2015. Digital stereo photogrammetry for grain-scale monitoring of fluvial surfaces: error evaluation and workflow optimisation. *ISPRS J. Photogramm. Remote Sens.* 101, 193–208. <http://dx.doi.org/10.1016/j.isprsjprs.2014.12.019>.
- Besl, P.J., McKay, N.D., 1992. Method for registration of 3-D shapes. *Robotics-DL Tentative. International Society for Optics and Photonics*, pp. 586–606. <http://dx.doi.org/10.1117/12.57955>.
- Brasington, J., Smart, R., 2003. Close range digital photogrammetric analysis of experimental drainage basin evolution. *Earth Surf. Process. Landf.* 28, 231–247. <http://dx.doi.org/10.1002/esp.480>.
- Brasington, J., Vericat, D., Rychkov, I., 2012. Modeling river bed morphology, roughness, and surface sedimentology using high resolution terrestrial laser scanning. *Water Resour. Res.* 48, <http://dx.doi.org/10.1029/2012WR012223>.
- Braudrick, C.A., Dietrich, W.E., Leverich, G.T., Sklar, L.S., 2009. Experimental evidence for the conditions necessary to sustain meandering in coarse-bedded rivers. *Proc. Natl. Acad. Sci. U. S. A.* 106, 16936–16941. <http://dx.doi.org/10.1073/pnas.0909417106>.
- Brush, L.M., Wolman, M.G., 1960. Knickpoint behavior in noncohesive material: a laboratory study. *Geol. Soc. Am. Bull.* 71, 59–74. [http://dx.doi.org/10.1130/0016-7606\(1960\)71\[59:KBINMA\]2.0.CO;2](http://dx.doi.org/10.1130/0016-7606(1960)71[59:KBINMA]2.0.CO;2).
- Butler, J.B., Lane, S.N., Chandler, J.H., 2001. Automated extraction of grain-size data from gravel surfaces using digital image processing. *J. Hydraul. Res.* 39, 1–11. <http://dx.doi.org/10.1080/00221686.2001.9628276>.
- Cavalli, M., Tarolli, P., Marchi, L., Dalla Fontana, G., 2008. The effectiveness of airborne LiDAR data in the recognition of channel-bed morphology. *Catena* 73, 249–260. <http://dx.doi.org/10.1016/j.catena.2007.11.001>.
- Chandler, J.H., Shiono, K., Rameshwaran, P., Lane, S.N., 2001. Measuring flume surfaces for hydraulics research using a Kodak DCS460. *Photogramm. Rec.* 17, 39–61. <http://dx.doi.org/10.1111/0031-868X.00167>.
- Ettema, R., Armstrong, D.R., Thornton, C.I., Hughes, S.A., Abt, S.R., 2016. Hydraulic modeling of braided channels self-formed in an alluvial plain. In: Constantinescu, G., Garcia, M., Hanes, D. (Eds.), *River Flow 2016*. CRC Press-Taylor & Francis Group, pp. 1106–1112.
- Faro, 2011. Faro Laser Scanner Focus3D.. (Technical Sheet).
- Finnegan, N.J., Sklar, L.S., Fuller, T.K., 2007. Interplay of sediment supply, river incision, and channel morphology revealed by the transient evolution of an experimental bedrock channel. *J. Geophys. Res.* 112, <http://dx.doi.org/10.1029/2006JF000569>.
- Fonstad, M.A., Dietrich, J.T., Courville, B.C., Jensen, J.L., Carboneau, P.E., 2013. Topographic structure from motion: a new development in photogrammetric measurement. *Earth Surf. Process. Landf.* 38, 421–430. <http://dx.doi.org/10.1002/esp.3366>.
- Furukawa, Y., Ponce, J., 2010. Accurate, dense, and robust multiview stereopsis. *IEEE Trans. Pattern Anal. Mach. Intell.* 32, 1362–1376. <http://dx.doi.org/10.1109/TPAMI.2009.161>.
- Gilbert, G.K., Murphy, E.C., 1914. *The Transportation of Debris by Running Water*. 86. US Government Printing Office.
- Girardeau-Montaut, D., 2011. CloudCompare (version 2.6.2): 3D point cloud and mesh processing software. (accessed 30 January 2016). <http://www.danielgm.net/cc/>.
- Humphries, R., Venditti, J.G., Sklar, L.S., Wooster, J.K., 2012. Experimental evidence for the effect of hydrographs on sediment pulse dynamics in gravel-bedded rivers. *Water Resour. Res.* 48, <http://dx.doi.org/10.1029/2011WR010419>.
- James, M., Robson, S., 2012. Straightforward reconstruction of 3D surfaces and topography with a camera: accuracy and geoscience application. *J. Geophys. Res. Earth Surf.* (2003–2012) 117, <http://dx.doi.org/10.1029/2011JF002289>.
- Johnson, J.P., Whipple, K.X., 2007. Feedbacks between erosion and sediment transport in experimental bedrock channels. *Earth Surf. Process. Landf.* 32, 1048–1062. <http://dx.doi.org/10.1002/esp.1471>.
- Kasprak, A., Wheaton, J.M., Ashmore, P.E., Hensleigh, J.W., Peirce, S., 2015. The relationship between particle travel distance and channel morphology: results from physical models of braided rivers. *J. Geophys. Res. Earth Surf.* 120, 55–74. <http://dx.doi.org/10.1002/2014JF003310>.
- Kim, H.S., Kimura, I., Shimizu, Y., 2015. Bed morphological changes around a finite patch of vegetation. *Earth Surf. Process. Landf.* 40, 375–388. <http://dx.doi.org/10.1002/esp.3639>.
- Kuhnle, R.A., 1993. Incipient motion of sand-gravel sediment mixtures. *J. Hydraul. Eng.* 119, 1400–1415. [http://dx.doi.org/10.1061/\(ASCE\)0733-9429\(1993\)119:12\(1400\)](http://dx.doi.org/10.1061/(ASCE)0733-9429(1993)119:12(1400)).
- Lague, D., Brodin, N., Leroux, J., 2013. Accurate 3D comparison of complex topography with terrestrial laser scanner: application to the Rangitikei canyon (NZ). *ISPRS J. Photogramm. Remote Sens.* 82, 10–26. <http://dx.doi.org/10.1016/j.isprsjprs.2013.04.009>.
- Lane, S., Chandler, J., Porfiri, K., 2001. Monitoring river channel and flume surfaces with digital photogrammetry. *J. Hydraul. Eng.* 127 (10), 871–877. [http://dx.doi.org/10.1061/\(ASCE\)0733-9429\(2001\)127:10\(871\)](http://dx.doi.org/10.1061/(ASCE)0733-9429(2001)127:10(871).
- Lane, S., Richards, K., Chandler, J., 1993. Developments in photogrammetry: the geomorphological potential. *Prog. Phys. Geogr.* 17 (3), 306–328.
- Lanzoni, S., 2000a. Experiments on bar formation in a straight flume. 1. Uniform sediment. *Water Resour. Res.* 36, 3337–3350. <http://dx.doi.org/10.1029/2000WR900160>.
- Lanzoni, S., 2000b. Experiments on bar formation in a straight flume. 2. Graded sediment. *Water Resour. Res.* 36, 3351–3364. <http://dx.doi.org/10.1029/2000WR900161>.
- Leica, 2016. Leica HDS3000. . (accessed 30 January 2016). <http://hds.leica-geosystems.com/en/5574.htm>.
- Lisle, T.E., Iseye, F., Ikeda, H., 1993. Response of a channel with alternate bars to a decrease in supply of mixed-size bed load: a flume experiment. *Water Resour. Res.* 29, 3623–3629. <http://dx.doi.org/10.1029/93WR01673>.
- Lowe, D.G., 2004. Distinctive image features from scale-invariant keypoints. *Int. J. Comput. Vis.* 60, 91–110. <http://dx.doi.org/10.1023/B:VISI.0000029664.99615.94>.
- Marion, A., Tait, S.J., McEwan, I.K., 2003. Analysis of small-scale gravel bed topography during armoring. *Water Resour. Res.* 39, <http://dx.doi.org/10.1029/2003WR002367>.
- Marra, W.A., Braat, L., Baar, A.W., Kleinhans, M.G., 2014. Valley formation by groundwater seepage, pressurized groundwater outbursts and crater-lake overflow in flume experiments with implications for Mars. *Icarus* 232, 97–117. <http://dx.doi.org/10.1016/j.icarus.2013.12.026>.
- Marzolff, I., Poesen, J., 2009. The potential of 3D gully monitoring with GIS using high-resolution aerial photography and a digital photogrammetry system. *Geomorphology* 111, 48–60. <http://dx.doi.org/10.1016/j.geomorph.2008.05.047>.
- Micheletti, N., Chandler, J.H., Lane, S.N., 2015. Investigating the geomorphological potential of freely available and accessible structure-from-motion photogrammetry using a smartphone. *Earth Surf. Process. Landf.* 40, 473–486. <http://dx.doi.org/10.1002/esp.3648>.
- Nelson, P.A., Brew, A.K., Morgan, J.A., 2015. Morphodynamic response of a variable-width channel to changes in sediment supply. *Water Resour. Res.* 51, 5717–5734. <http://dx.doi.org/10.1002/2014WR016806>.
- Nelson, P.A., Dietrich, W.E., Venditti, J.G., 2010. Bed topography and the development of forced bed surface patches. *J. Geophys. Res.* 115, <http://dx.doi.org/10.1029/2010JF001747>.
- Nelson, P.A., Venditti, J.G., Dietrich, W.E., Kirchner, J.W., Ikeda, H., Iseye, F., Sklar, L.S., 2009. Response of bed surface patchiness to reductions in sediment supply. *J. Geophys. Res.* 114, <http://dx.doi.org/10.1029/2008JF001144>.
- Nouwakpo, S.K., James, M.R., Weltz, M.A., Huang, C.-H., Chagas, I., Lima, L., 2014. Evaluation of structure from motion for soil microtopography measurement. *Photogramm. Rec.* 29, 297–316. <http://dx.doi.org/10.1111/phor.12072>.
- Paschotta, R., 2008. *Encyclopedia of Laser Physics and Technology*. vol. 1. Wiley-VCH, Weinheim, Germany.
- Peter Heng, B., Chandler, J.H., Armstrong, A., 2010. Applying close range digital photogrammetry in soil erosion studies. *Photogramm. Rec.* 25, 240–265. <http://dx.doi.org/10.1111/j.1477-9730.2010.00584.x>.
- Prosdocimi, M., Calligaro, S., Sofia, G., Dalla Fontana, G., Tarolli, P., 2015. Bank erosion in agricultural drainage networks: new challenges from structure-from-motion photogrammetry for post-event analysis. *Earth Surf. Process. Landf.* 40, 1891–1906. <http://dx.doi.org/10.1002/esp.3767>.
- Qin, J., Ng, S.L., 2012. Estimation of effective roughness for water-worked gravel surfaces. *J. Hydraul. Eng.* 138, 923–934. [http://dx.doi.org/10.1061/\(ASCE\)HY.1943-7900.000610](http://dx.doi.org/10.1061/(ASCE)HY.1943-7900.000610).
- Ramos, P.X., Bento, A.M., Maia, R., Pêgo, J.P., 2015. Characterization of the scour cavity evolution around a complex bridge pier. *J. Appl. Water Eng. Res.* 1–10. <http://dx.doi.org/10.1080/23249676.2015.1090353>.
- Schumm, S., Khan, H., 1972. Experimental study of channel patterns. *Geol. Soc. Am. Bull.* 83, 1755–1770. [http://dx.doi.org/10.1130/0016-7606\(1972\)83\[1755:ESPOTC\]2.0.CO;2](http://dx.doi.org/10.1130/0016-7606(1972)83[1755:ESPOTC]2.0.CO;2).
- Sklar, L.S., Fadde, J., Venditti, J.G., Nelson, P., Wydzga, M.A., Cui, Y., Dietrich, W.E., 2009. Translation and dispersion of sediment pulses in flume experiments simulating gravel augmentation below dams. *Water Resour. Res.* 45, <http://dx.doi.org/10.1029/2008WR007346>.
- Smith, M., Carrivick, J., Quincey, D., 2015. Structure from motion photogrammetry in physical geography. *Prog. Phys. Geogr.* 1–29. <http://dx.doi.org/10.1177/0309133315615805>.
- Smith, M., 2014. Evaluating shallow-water bathymetry from through-water terrestrial laser scanning under a range of hydraulic and physical water quality conditions. *River Res. Appl.* 30, 905–924. <http://dx.doi.org/10.1111/phor.12072>.
- Smith, M.W., Vericat, D., 2015. From experimental plots to experimental landscapes: topography, erosion and deposition in sub-humid badlands from structure-from-motion photogrammetry. *Earth Surf. Process. Landf.* <http://dx.doi.org/10.1002/esp.3747>.
- Snavely, N., Seitz, S.M., Szeliski, R., 2006. Photo tourism: exploring photo collections in 3d. *ACM Transactions on Graphics (TOG)*. ACM, pp. 835–846.
- Stojic, M., Chandler, J., Ashmore, P., Luce, J., 1998. The assessment of sediment transport rates by automated digital photogrammetry. *Photogramm. Eng. Remote. Sens.* 64, 387–395.
- Tingdahl, D., Van Gool, L., 2011. A public system for image based 3D model generation. *Computer Vision/Computer Graphics Collaboration Techniques*. Springer, pp. 262–273. http://dx.doi.org/10.1007/978-3-642-24136-9_23.
- Ullman, S., 1979. The interpretation of structure from motion. *Proc. R. Soc. Lond. B Biol. Sci.* 203, 405–426. <http://dx.doi.org/10.1098/rspb.1979.0006>.

- van Dijk, W.M., van de Lageweg, W.I., Kleinhans, M.G., 2012. 8. Experimental meandering river with chute cutoffs. *J. Geophys. Res.* 117, <http://dx.doi.org/10.1029/2011JF002314>.
- Venditti, J.G., Lin, C.-Y.M., Kazemi, M., 2015. Variability in bedform morphology and kinematics with transport stage. *Sedimentology* 63, 1017–1040. <http://dx.doi.org/10.1111/sed.12247>.
- Venditti, J.G., Nelson, P.A., Minear, J.T., Wooster, J., Dietrich, W.E., 2012. Alternate bar response to sediment supply termination. *J. Geophys. Res.* <http://dx.doi.org/10.1029/2011JF002254>.
- Wackrow, R., Chandler, J.H., 2008. A convergent image configuration for DEM extraction that minimises the systematic effects caused by an inaccurate lens model. *Photogramm. Rec.* 23, 6–18. <http://dx.doi.org/10.1111/j.1477-9730.2008.00467.x>.
- Wackrow, R., Chandler, J.H., 2011. Minimising systematic error surfaces in digital elevation models using oblique convergent imagery. *Photogramm. Rec.* 26, 16–31. <http://dx.doi.org/10.1111/j.1477-9730.2011.00623.x>.
- Wang, C., Wang, Q., Meire, D., Ma, W., Wu, C., Meng, Z., Van de Koppel, J., Troch, P., Verhoeven, R., De Mulder, T., et al. 2016. Biogeomorphic feedback between plant growth and flooding causes alternative stable states in an experimental floodplain. *Adv. Water Resour.* 93, 223–235. <http://dx.doi.org/10.1016/j.advwatres.2015.07.003>.
- Westoby, M., Brasington, J., Glasser, N., Hambrey, M., Reynolds, J., 2012. ‘Structure-from-motion’ photogrammetry: a low-cost, effective tool for geoscience applications. *Geomorphology* 179, 300–314. <http://dx.doi.org/10.1016/j.geomorph.2012.08.021>.
- Wu, C., 2013. Towards linear-time incremental structure from motion. 2013 International Conference on 3D Vision-3DV 2013. IEEE., pp. 127–134. <http://dx.doi.org/10.1109/3DV.2013.25>.
- Wu, C., Agarwal, S., Curless, B., Seitz, S.M., 2011. Multicore bundle adjustment. 2011 IEEE Conference on Computer Vision and Pattern Recognition (CVPR). IEEE., pp. 3057–3064. <http://dx.doi.org/10.1109/CVPR.2011.5995552>.